Chapter 5

Deformation and Recrystallization Behaviors in Magnesium Alloys

Jae-Hyung Cho and Suk-Bong Kang

Additional information is available at the end of the chapter

http://dx.doi.org/10.5772/55597

1. Introduction

Magnesium alloys have a great potential for application to lightweight structural components due to their low density, high specific strength and stiffness. In particular, wrought Mg alloys have attracted much attention due to their more advantageous mechanical properties compared to cast Mg alloys. The strong preferred orientations, mechanical planar anisotropy, and thus the poor formability of wrought magnesium alloys at room temperature, however, prevent their wider use in areas such as automotive and aerospace parts, electronic devices, and consumable products. These disadvantages are mainly attributed to their hcp (hexagonal close packed) structure and the associated insufficient independent slip systems.

Various studies of wrought magnesium alloys have focused on a microstructure modification of the fine grains and off-basal texturing to improve their formability by means of alloy designs and appropriate forms of thermo-mechanical processing. Alloying designs, which mainly incorporate rare-earth metals, have been used to obtain better off-basal texturing [1–4]. Deviation from the strong basal texture by extrusion [5, 6] and equal-channel angular extrusion (ECAE) processes [7] has been shown to enhance the formability. The weakening of the basal textures was also observed during an asymmetric rolling process [8–13], which resulted in better elongation.

Table 1 shows the frequently-found deformation modes in magnesium alloys, including both slip and twinning systems. The critical resolved shear stresses (CRSS) of non-basal slip systems such as prismatic and pyramidal slip systems show much higher values at room temperature than those of basal slip systems [14, 15]. These hinder the strong activation of the deformation modes enough to accommodate external loading or plastic deformation at room temperature, finally resulting in poor formability. The basal $\langle a \rangle$ system, which is mainly activated at room temperature, does not fully accommodate

external elongation, although tensile twinning offers lattice reorientation and further adjusts the degree of deformation. The CRSS of magnesium alloys commonly varies with the temperature. Particularly, non-basal slip systems are more sensitive to temperature, and the CRSS in those cases quickly decreases with the temperature. The activation of non-basal slip systems at elevated temperatures improves the formability of magnesium alloys. The various misorientation relationships between the matrix and the twins commonly observed during the microstructural evolution of Mg alloys are summarized in Table 2.

Deformation mode	$\{hki\bar{l}\}\langle uvt\bar{w}\rangle$
Basal $\langle a\rangle$	$\{0002\}\langle 11\bar{2}0\rangle$
Prismatic $\langle a\rangle$	$\{1\bar{1}00\}\langle 11\bar{2}0\rangle$
Pyramidal $\langle c+a\rangle$	$\{11\bar{2}\bar{2}\}\langle 11\bar{2}3\rangle$
Tensile twin	$\{10\bar{1}2\}\langle 10\bar{1}\bar{1}\rangle$
Compressive twin	$\{10\bar{1}1\}\langle 10\bar{1}\bar{2}\rangle$

Table 1. Various deformation modes in magnesium alloys.

Twin type	**Misorientation angle/axis**	
$\{10\bar{1}1\}$	$56°\langle 1\bar{2}10\rangle$	compressive twin
$\{10\bar{1}2\}$	$86°\langle 1\bar{2}10\rangle$	tensile twin
$\{10\bar{1}3\}$	$64°\langle 1\bar{2}10\rangle$	
$\{10\bar{1}1\}-\{10\bar{1}2\}$	$38°\langle 1\bar{2}10\rangle$	double twin
$\{10\bar{1}3\}-\{10\bar{1}2\}$	$22°\langle 1\bar{2}10\rangle$	

Table 2. Twinning misorientations commonly observed in magnesium alloys

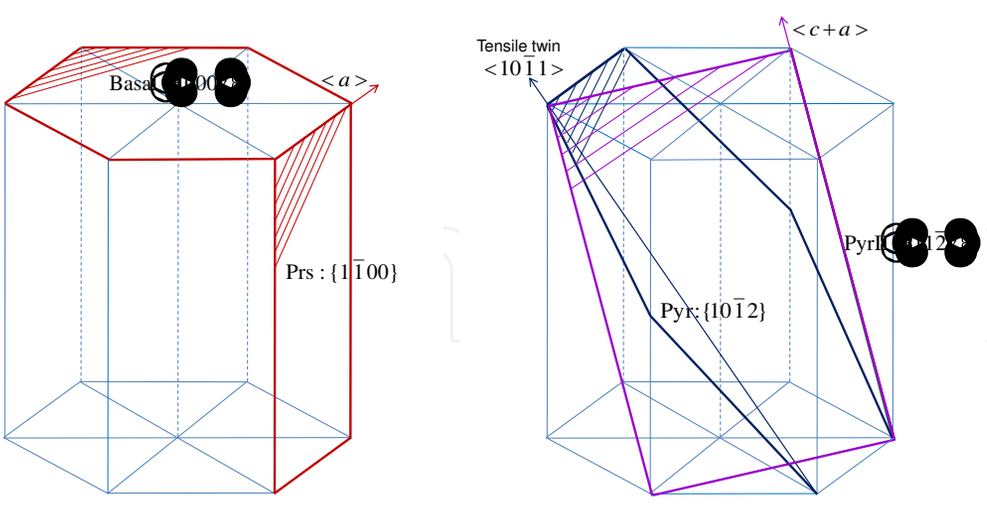

(a) (b)

Figure 1. Lattice planes and directions of the hexagonal crystal structure: (a) basal and prismatic planes, and (b) pyramidal planes

http://dx.doi.org/10.5772/55597

For magnesium alloys, the most dominant deformation mode is the basal ⟨a⟩ slip system regardless of the temperature. The basal ⟨a⟩ slip system is usually aligned with the deformation direction. It aligns the c-axis to the plane normal direction (ND) of the sheet during the rolling process [13]. Similarly, the c-axis vertically aligns to the extrusion direction of the billets during extrusion [6, 16]. The extrusion process contains axisymmetric deformation along the extrusion direction. Most thermo-mechanical processing methods of Mg alloys are carried out at elevated temperatures due to the limited slip system at room temperature. The warm- or hot-working processes frequently cause complex microstructural changes due to dynamic recrystallization in addition to deformation. The rolled sheets or extruded billets should also be annealed to relax the stored energy and to improve the degree of microstructural inhomogeneity for the next forming process.

Here, we present the textural and microstructural evolution during the deformation and recrystallization of various magnesium alloys. Mechanical responses corresponding to the microstructure are also discussed. Uniaxial compression and rolling processes followed by annealing were used as case studies.

2. Experiments

2.1. Materials

Four different magnesium alloys of extruded AZ31B (Mg-Al-Zn system), twin-roll casted AZ31B, ingot-casted ZK60 (Mg-Zn-Zr system) and ingot-casted AM31 (Mg-Al-Mn system) alloys were studied. The overall chemical compositions of the materials are presented in Table 3.

For uni-axial compression tests, cylindrical extruded AZ31B billets and ingot-casted ZK60 alloys were used. Through the compression tests, the deformation and mechanical responses were discussed. The extruded AZ31B billets were commercially fabricated and had an initial diameter of 9 mm. They were simply cut into compression samples with a length of 12 mm.

The other compression samples were prepared using ingot-casted ZK60 alloys, which were originally fabricated by conventional direct chill casting (DC) in a laboratory scale. Its initial thickness was approximately 20 mm and it was warm-rolled down to 15 mm, and then solution heat-treated at 673 K (400 °C) for 15 hours (T4). ZK60 billets with a thickness of 15 mm were machined into cylindrical samples for uniaxial compression. Figure 2 depicts the sample geometry obtained from the initial 15 mm-thick ingot. The character *V* referes to the vertical direction and *H*, denotes the horizontal direction. The V_0, V_{45} and V_{90} samples were machined from the rolling direction (RD) to the ND in each case. The numbers 0, 45, and 90 refer to the angles between the RD and the particular sample used. The ZK60 alloys are typical magnesium alloys with aging (precipitation) hardening, where their strength levels also change with aging [17–21]. Here, we focus on the solid solution state (T4) of the ZK60 alloys. A more detailed discussion of ZK60 alloys including both solid-solution (T4) and artificial-aging (T6) states will be given later.

The AZ31B strips fabricated by twin-roll casting and the ingot-casted AM31 alloys were used for warm-rolling and subsequent annealing. These were also fabricated at a laboratory scale. The initial thickness of the AZ31B strips was about 5 mm, and it was warm-rolled down to about 2 mm, as suggested in the literature [22]. The initial thickness of the ingot-casted

AM31 alloys was 20 mm. The discussion pertaining to the recrystallization behaviors was based on the warm-rolling and annealing processes of the AM31 and AZ31B samples.

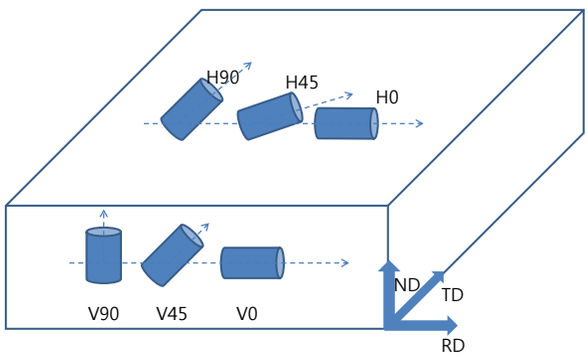

Figure 2. Uniaxial samples taken from the ZK60 billet along various directions with regard to the rolling direction (RD) and normal direction (ND). V_0, V_{45} and V_{90} represent the samples taken from the RD to the ND, while H_0, H_{45} and H_{90} represent the samples taken from the RD to the transverse direction (TD).

2.2. Thermo-mechanical processing

Uniaxial compression tests were carried out using the Thermecmastor-Z (Fuji Electronic Industrial Co.). Cylindrical AZ31B billets with a diameter of 9 mm and a length of 12 mm were used for the compression tests. The other alloys, ZK60 alloys, were machined into compression samples 12 mm in length and 8 mm in diameter, as shown in Fig. 2.

The deformation temperatures of the AZ31B billets were 473 K (200 °C), 523 K (250 °C), and 573 K (300 °C), while the strain rates were 0.00139/s and 0.139/s. Ex-situ experiments to determine the microstructural evolution were also carried out at a temperature of 523 K (250 °C) and a strain rate of 0.32/s. For the ex-situ compression, the sample was marked with micro-indentations and compression and EBSD measurements were then alternately repeated.

Uniaxial compression tests for the ZK60 alloys were also carried out at various temperatures and strain rates. Wider deformation temperatures were imposed on the ZK60 alloys than on the AZ31B samples, and the temperatures were 298 K (25 °C), 398 K (125 °C), 448 K (175 °C), 498 K (225 °C), 548 K (275 °C), 598 K (325 °C), and 698 K (425 °C). Two different strain rates were used, 0.0069/s and 0.139/s. At total strain values of 3% and 7% at a strain rate of 0.139/s, microstructural mapping was carried out using EBSD. Each cylindrical sample was prepared according to the specimen preparation sequence for EBSD mapping before compression, after which the uniaxial compression and EBSD mapping were repeated alternately to determine the microstructural evolution during compression.

Figure 3 shows a schematic diagram of the cylindrical sample and the EBSD measurement region. The extrusion direction is parallel to the compression direction. The orientation color code of the EBSD inverse pole figure maps is also shown.

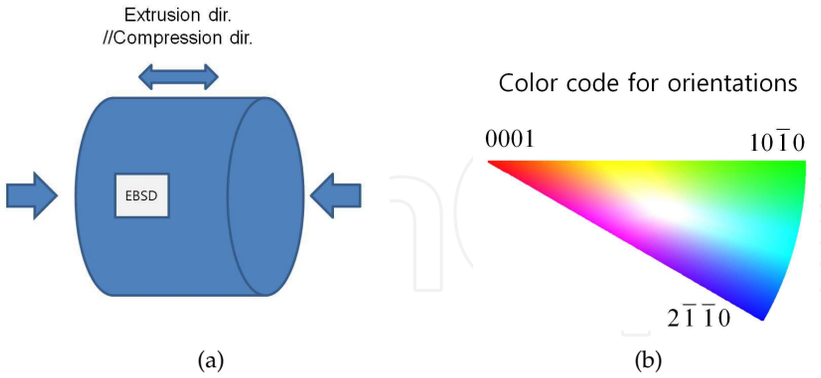

Figure 3. Sample geometry for EBSD measurements (a), and orientation color code of the inverse pole figure maps (IPFs) (b)

Element	Al	Zn	Mn	Si	Cu	Ca	Fe	Ni	Zr	Mg
AZ31B	2.5-3.5	0.6-1.4	0.2-1.0	< 0.1	< 0.05	< 0.04	< 0.005	< 0.005	-	Bal.
ZK60	0.01	5.47	0.009	0.022	0.003	0.005	0.003	0.007	0.58	Bal.
AM31	3.3	-	0.8	-	-	-	-	-	-	Bal.

Table 3. Chemical composition of AZ31B, ZK60 and AM31 alloys used[wt%].

Ingot-casted AM31 alloys were hot-rolled at 673 K (400 °C) for a reduction in area of about 5% and the microstructure of the as-rolled state was measured using EBSD. AZ31B sheets with an initial thickness of 2 mm were warm-rolled down to 1 mm at a temperature of 498 K (225 °C). The average reduction in area per rolling pass was approximately 10%, and the total reduction in area was 50%. Static annealing was carried out on the warm-rolled AZ31B sheets for 10 min at 573 K (300 °C). The warm-rolling was carried out using a rolling mill with a diameter of 280 mm. The intermediate annealing time between each pass was about 5 min. No lubrication was applied.

2.3. Microstructure characterization

Characterization of the microstructure and texture was mainly carried out using EBSD (electron backscatter diffraction). An automated HR-EBSD (JEOL7001F) with a HKL Channel-5 and the generalized EBSD data analysis code REDS [23] were both used. EBSD samples were mechanically polished and then electropolished using a solution of butyl cellosolve (50 ml), ethanol (10 ml) and perchloric acid (5 ml) at a voltage of 10 V and at temperatures ranging from 253 K (−20 °C) to 258 K (−15 °C).

3. Deformation of Mg alloys

Textural and microstructural evolution and associated mechanical responses were investigated during the uniaxial compression of the Mg alloys at various temperatures and strain rates. Two different Mg alloys of extruded AZ31B billets and ingot-casted ZK60 alloys were prepared for the mechanical tests.

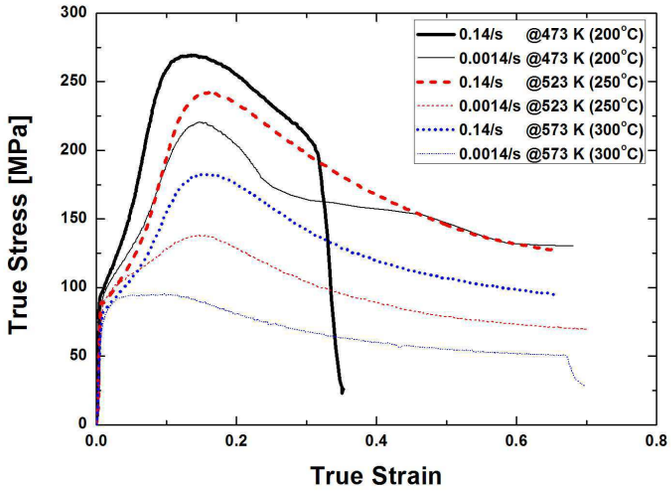

Figure 4. Uniaxial compression of extruded AZ31B billets at various temperatures and deformation rates

3.1. Extruded AZ31B billets

Figure 4 shows the flow curves of the extruded AZ31B billets during uniaxial compression. All three temperatures of 473 K (200 °C), 523 K (250 °C), and 573 K (300 °C) show the peak strength values, after which they decrease with the strain. With an increase in the compression temperature from 473 K (200 °C) to 573 K (300 °C), the peak strength also gradually decreases. The peak value in the strength implies some dynamic process during compression at that temperature and strain rate. The highest peak strength is found at a strain rate of 0.14/s and a temperature of 473 K (200 °C). Even at the same temperature, the lower deformation rate of 0.0014/s results in a low value of the peak strength. When considering the elongation during compression at 473 K (200 °C), the high deformation rate of 0.14/s results in a rapid failure at around 35%. In contrast, the low deformation rate of 0.0014/s reveals a more active dynamic process and the elongation continues, reaching more than 60% past the peak strength. As expected, the lowest strength is observed at a strain rate of 0.0014/s and a temperature of 573 K (300 °C). Overall, high temperature conditions of 523 K (250 °C) and 573 K (300 °C) enhance the elongation until it is greater than 60%.

Ex-situ EBSD measurements of the extruded AZ31B billets during uniaxial compression were carried out on the side, with the samples polished until they had a flat surface, as shown in Fig. 3. Figure 5 shows the flow curve with the ex-situ EBSD measuring points of the extruded AZ31B billets shown in Fig. 5. Open circles illustrate the various strains corresponding to the EBSD measurements. The EBSD measurements were taken of the sample before the peak strength.

Figure 6 presents the textural and microstructural evolution during the uniaxial compression of the extruded AZ31B billets. Micro-indentations were used to identify the mapping area during deformation. The initial microstructure reveals some mixture of large and small grains from the inverse pole figure (IPF) map shown in Fig. 6(a). The IPF maps were plotted based on the extrusion direction (ED), and thus both blue and green on the IPF imply that the $\langle 2\bar{1}\bar{1}0 \rangle$ and the $\langle 10\bar{1}0 \rangle$ directions align to the ED, respectively. Note the Fig. 3(b).

http://dx.doi.org/10.5772/55597

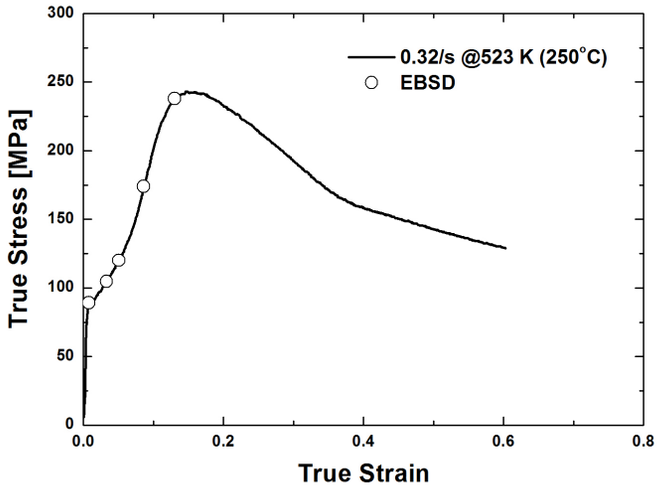

Figure 5. Flow curve with the ex-situ EBSD mapping points of extruded AZ31B billets

The extruded AZ31B billets contained typical extrusion textures. The texture and microstructure quickly changed upon deformation. Twinning activity was evident during compression. Approximately, a strain of 3% caused most of the blue and green grains to contain tensile twinning, which denotes a $\{10\bar{1}2\}\langle 10\bar{1}0\rangle$ or $86°\langle 1\bar{2}10\rangle$ misorientation relationship. At a strain of 5%, twinning grew very fast. Nearly the entire region underwent twinning at a strain of 8%. As the deformation degree increased, the EBSD inverse pole figure contained more of a non-indexed region, as shown in black. Grain boundary maps are also presented in Fig. 7. A grain identification (GID) angle of 15 ° is denoted by the thick lines and the GID of 2 ° is denoted by the thin lines.

Reorientation of the grains during uniaxial compression can also be found easily using pole figures (PFs), as shown in Fig 8. The coordinates of X_0 and Y_0 correspond to the extrusion (ED) or compression (CD), and the transverse (TD) directions, respectively. As-extruded billets have a fiber texture along the TD, which is typical in the texturing of extruded samples. This stems from the grain reorientation during uniaxial compression, in which the basal planes are parallel to the billet surface. With an increase of the deformation, many tensile twins occurred and grew into parent regions. Strong intensity near the X_0 or ED direction reflects the twinning. The maximum intensity in the pole figures also increases with the deformation.

Misorientation angle distributions are shown in Fig. 9. The solid line represents the misorientation angle distribution of randomly orientated hexagonal polycrystals. The as-received billets show a distribution similar to that of a random distribution. At a strain of 1%, a strong peak arises around a misorientation angle of 86°, which is associated with tensile twinning. This was most frequently observed at a strain of 3%, after which the frequency of low misorientation angles of less than 15° gradually increases. At a strain of 13%, a great amount of low angle frequency develops.

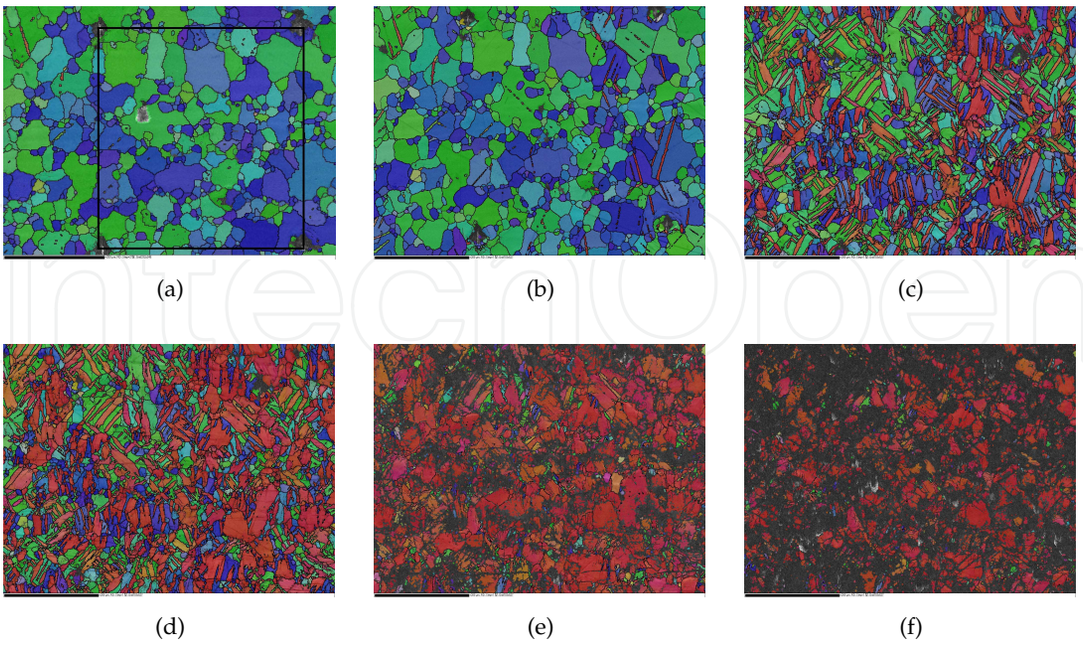

Figure 6. Inverse pole figure maps (IPFs) obtained along the extrusion direction (ED) or compression direction (CD) of the AZ31B billets. The grain identification angle (GID) is 15°. The step size for the EBSD measurements is 2 μm for as-extruded sample and 1 μm for others, and the scale bar at the bottom of the IPF maps is 200 μm. (a) as-extruded, (b) 1%, (c) 3%, (d) 5%, (e) 8%, and (f) 13%

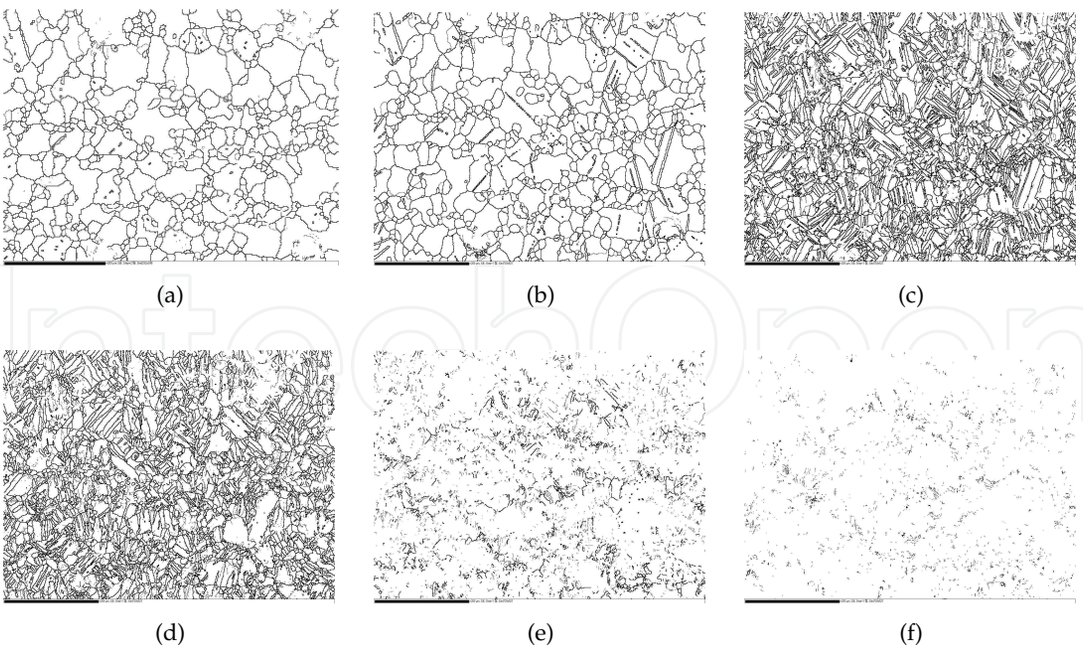

Figure 7. Grain boundary maps obtained from EBSD mapping (AZ31B billets). The grain identification angle (GID) is 15°. The step size for the EBSD measurements is 2 μm for as-extruded sample and for others 1 μm and the scale bar at the bottom of the IPF maps is 200 μm. (a) as-extruded, (b) 1%, (c) 3%, (d) 5%, (e) 8%, and (f) 13%

http://dx.doi.org/10.5772/55597

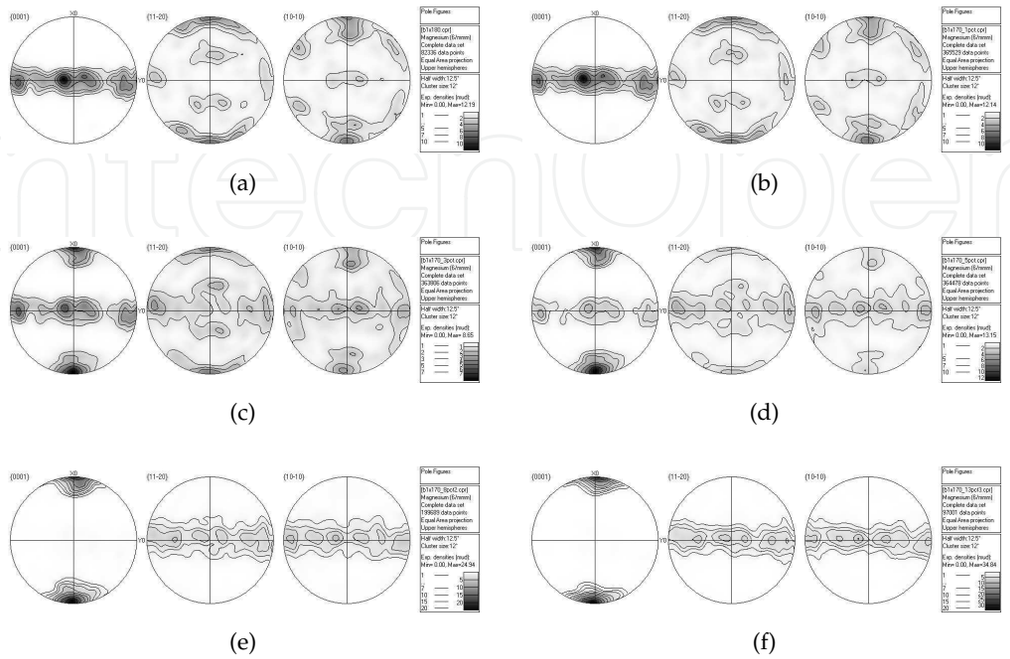

Figure 8. Pole figures obtained from EBSD mapping (AZ31B billets). The coordinates of X_0 and Y_0 correspond to the extrusion (ED) or compression (CD), and the transverse (TD) directions, respectively. (a) as-extruded, (b) 1%, (c) 3%, (d) 5%, (e) 8%, and (f) 13%

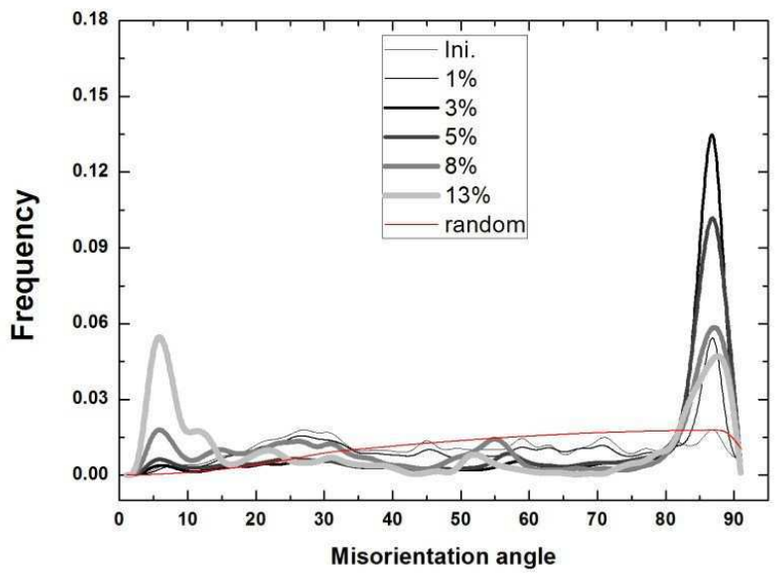

Figure 9. Misorientation distribution obtained from EBSD mapping (AZ31B billets).

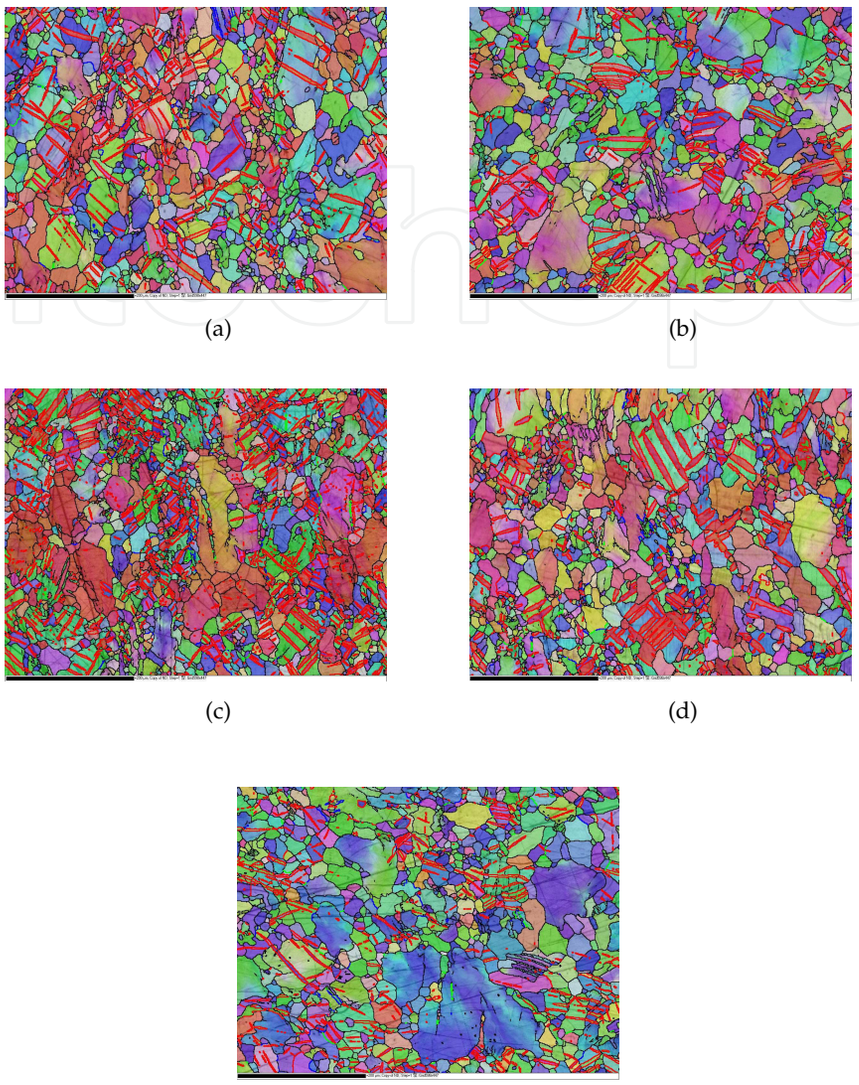

Figure 10. Inverse pole figure (IPF) maps obtained along the extrusion direction (ED) or compression direction (CD) of the ZK60 alloys ($\varepsilon = 3\%$, $\dot{\varepsilon} = 0.139/s$). The grain identification angle (GID) is 15°. The step size for the EBSD measurements is 1 μm, and the scale bar at the bottom of the IPF maps is 200 μm. (a) 448 K (175 °C), (b) 498 K (225 °C), (c) 548 K (275 °C), (d) 598 K (325 °C), and (e) 698 K (425 °C)

3.2. Ingot-casted ZK60 billets

The initial microstructure of the ingot-casted ZK60 alloys possessed an equi-axed grain structure with a weak basal texture.

During the uniaxial compression of the ZK60 alloys, the microstructural and textural evolution was investigated with the temperature. Figure 10 shows inverse pole figure maps of ZK60 at a strain and strain rate of 3% and 0.139/s, respectively. Tensile twinning boundaries are specified in red.

http://dx.doi.org/10.5772/55597

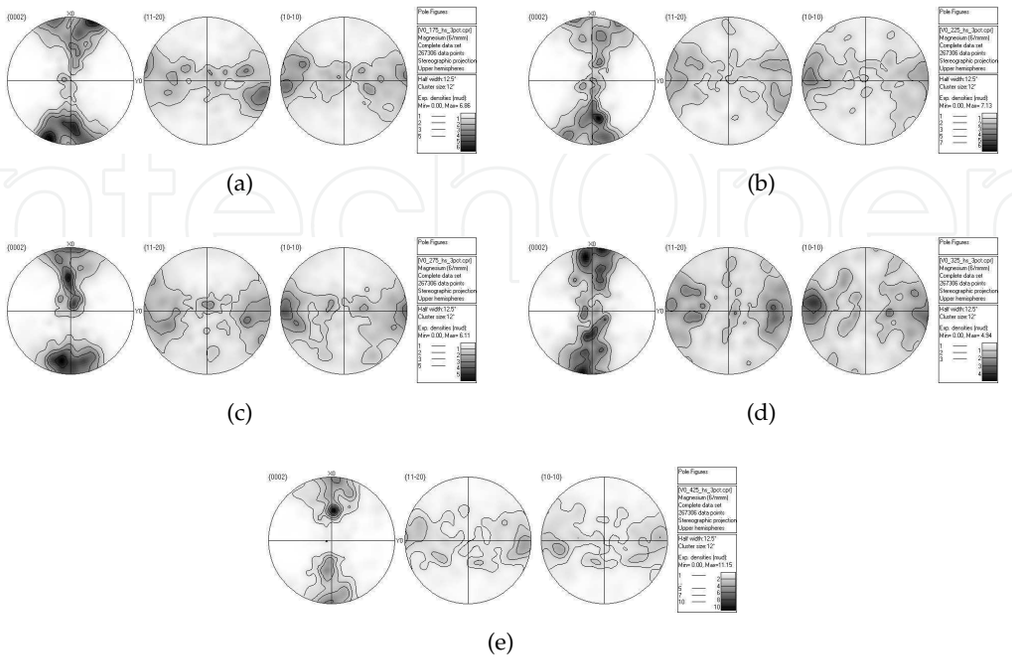

Figure 11. Pole figures of ZK60 alloys obtained from EBSD mapping ($\varepsilon = 3\%$, $\dot{\varepsilon} = 0.139$/s). The coordinates of X_0 and Z_0 correspond to the RD and extrusion direction (ED), respectively. (a) 448 K (175 °C), (b) 498 K (225 °C), (c) 548 K (275 °C), (d) 598 K (325 °C), and (e) 698 K (425 °C)

The variation of the basal intensity is more evident in Fig. 11, which shows pole figures computed from the EBSD mapping in Fig. 10. The initial sample showed weak basal intensity along the X_0 or the normal direction (ND) of the initial billet, as shown in Fig. 2. During compression, the grains were reoriented into the center of the pole figures, Z_0, or in the extrusion direction (ED). With an increase in the temperature, the overall basal intensity decreased. At a temperature of 698 K (425 °), the twinned region is small and the basal intensity in the center is comparatively low. It was noted that a high temperature affects twinning activation and propagation during compression, as less twinning was observed, as shown in Fig. 11(e). Note that the intensity in the center of the pole figure only appears slight in Fig. 11(e). Strong twinning activity results in a sharp increase in the basal intensity, which appears in the center of the (0002) pole figure. The maximum intensity found in Fig. 11(e) is associated with the initial large grains in Fig. 10(e), not with textural evolution due to compression. In fact, a texture analysis using EBSD mapping contains some statistical uncertainty coming from spatial limitations, and statistical uncertainty should therefore be assumed, unlike in the XRD texture analysis, which usually covers a large area and numerous grains.

The grain structure at a strain of 7% resulted in finer grains, as shown in Fig. 12, than that at a strain of 3 %, as shown in Fig. 10. Strong twinning activation and basal slip up to 598 K (325 °C) seem to increase the basal intensity further; thus, most grains appear in red, a result that is related to the basal fiber. In fact, more complicated activation of various deformation modes shown in Table 1 occurs during compression. Note that at a temperature of 698 K

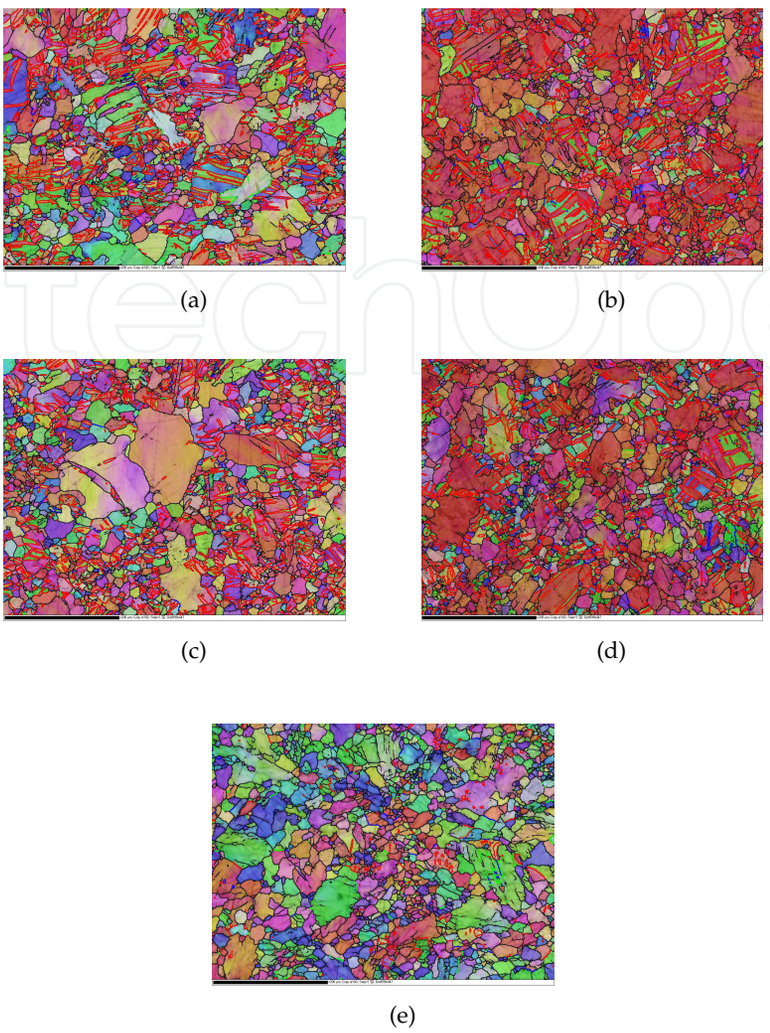

Figure 12. Inverse pole figure (IPF) maps obtained along the extrusion direction (ED) or compression direction (CD) of the ZK60 alloys ($\varepsilon = 7\%$, $\dot{\varepsilon} = 0.139$/s). The grain identification angle (GID) is 15°. The step size for the EBSD measurements is 1 μm, and the scale bar at the bottom of the IPF maps is 200 μm. (a) 448 K (175 °C), (b) 498 K (225 °C), (c) 548 K (275 °C), (d) 598 K (325 °C), and (e) 698 K (425 °C)

(425 °C), twinning activation is also weakest among other temperature conditions, as shown in at a strain of 3% in Fig. 11(e). Pole figures for the EBSD mapping data in Fig. 12 are shown in Fig. 13. Compared to the PFs at a low strain of 3% in Fig. 11, basal intensity in the center of the pole figures is much more evident in Fig. 13. It was also found that some variation arises in the maximum intensity as the temperature changes. The greatest maximum intensity among the PFs is observed in Fig. 13(c), and this appears to be related to the initially large grains, as discussed in Fig. 11(e).

The misorientation angle distributions at strains of 3% and 7% are given in Fig. 14. A very typical angle distribution is found. The most dominant frequency is observed near tensile twinning. At a large strain of 7%, a higher frequency occurs with misorientation angles smaller than 15°. This is related to the subgrain boundaries due to increase in plastic strain.

http://dx.doi.org/10.5772/55597

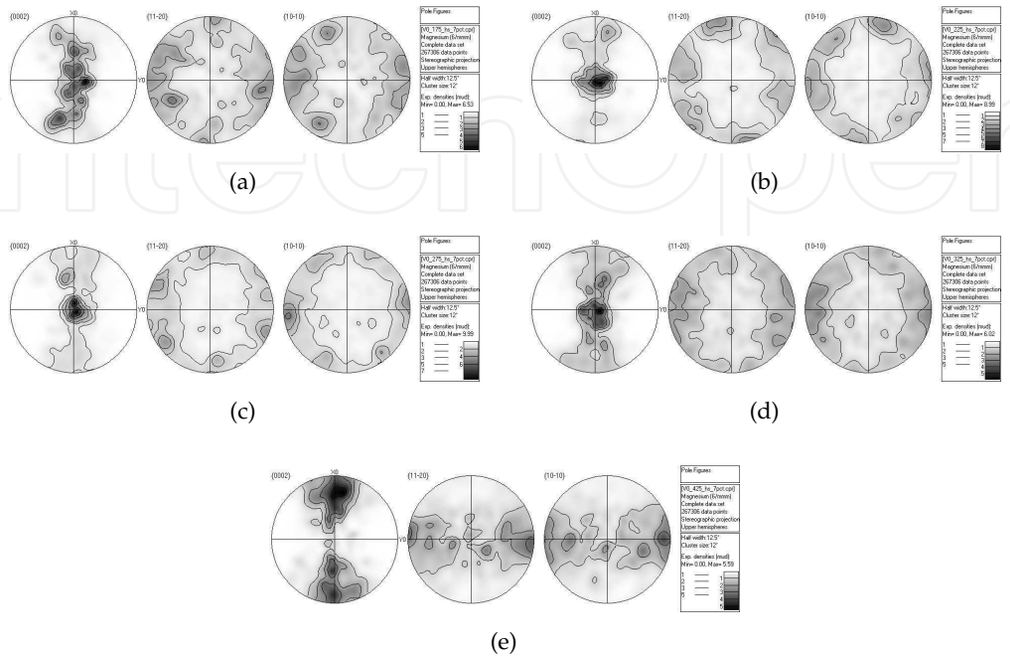

Figure 13. Pole figures of ZK60 alloys obtained from EBSD mapping ($\varepsilon = 7\%$, $\dot{\varepsilon} = 0.139/s$). The coordinates of X_0 and Z_0 correspond to the RD and extrusion direction (ED), respectively. (a) 448 K (175 °C), (b) 498 K (225 °C), (c) 548 K (275 °C), (d) 598 K (325 °C), and (e) 698 K (425 °C)

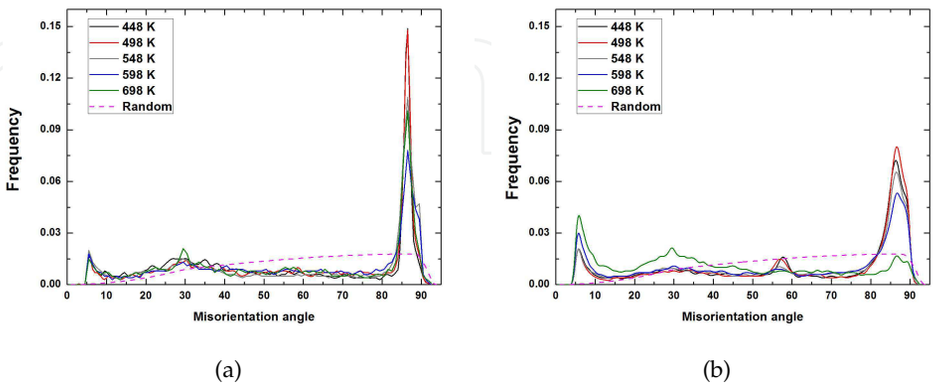

Figure 14. Misorientation distributions obtained from the EBSD mapping of ZK60. (a) ε = 3% (Fig. 10) and (b) ε = 7% (Fig. 12)

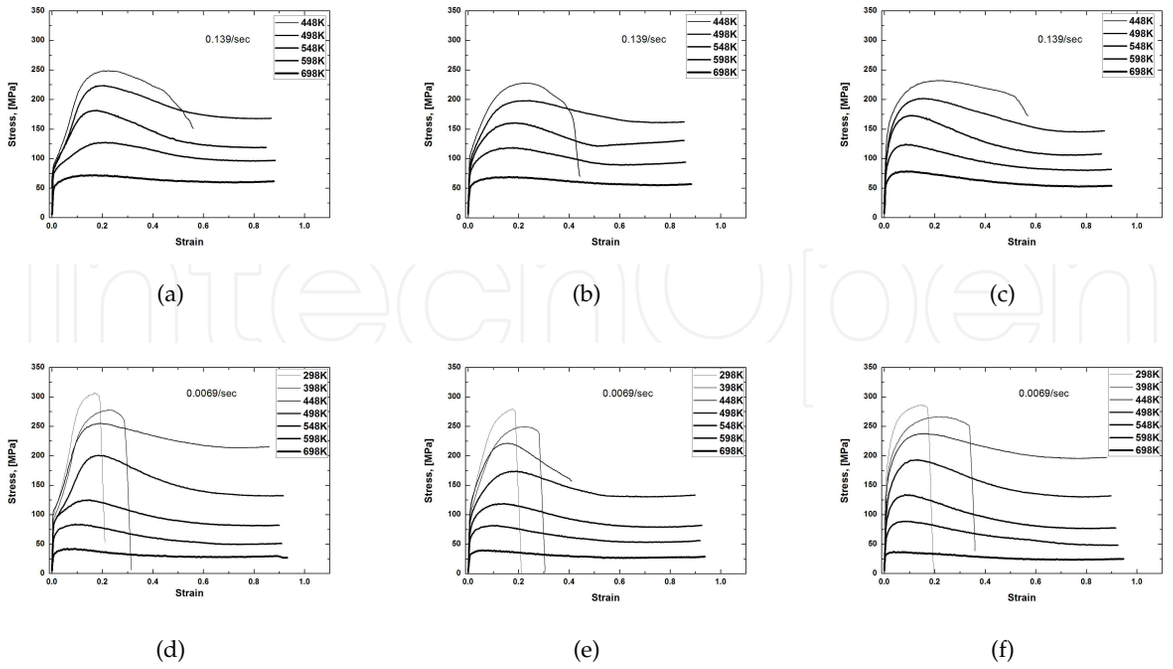

Figure 15. Flow curves obtained from ZK60 alloys. (a) V0, (b) V45, and (c) V90 at a deformation rate of 0.139/s. (d) V0, (e) V45, and (f) V90 at a deformation rate of 0.0069/s.

The flow curves obtained during the uniaxial compression of the ZK60 alloys along the vertical direction are shown in Fig. 15. There are some differences between a high strain rate (0.139/s) and a low strain rate (0.0069/s). For a low strain rate of 0.0069/s, low temperatures of 298 K (25 °C) and 398 K (125 °C) were additionally assessed. The low temperatures cannot provide enough deformation modes, and the elongation at the temperatures is less than it is at other temperatures. The high strain rate of 0.139 imparts higher strength than that at the low strain rate of 0.0069. At a temperature of 448 K (175 °C), it is clear that a strain of 0.0069 shows more extended elongation than a strain of 0.139. The flow curves in Fig. 15(a) correspond to the microstructures examined above in Figs. 10 and 12. The samples taken from the different direction respond differently to external loading or compression. The samples referred to as V_0 show the most dominant twinning; thus, some stress relaxation occurs during hardening (Figs. 15(a) and 15(d)). The samples termed V_{45} revealed some linear strain-hardening behavior (Figs. 15(b) and 15(e)). The samples referred to as V_{90} demonstrated typical non-linear strain-hardening behavior of the type usually found during the plastic deformation of polycrystalline materials (Figs. 15(c) and 15(f)). Note the curvature of the non-linear strain-hardening regions in the flow curves between V_0 and V_{90}. The former shows negative curvature, while the latter shows positive curvature.

Other flow curves obtained along the horizontal direction are shown in Fig. 16. At a high temperature of 498 K, the elongation is better than it is at a low temperature of 448 K. The strain-hardening behaviors of all samples measured from the horizontal directions, H_0, H_{45}, and H_{90}, are similar to those of V_0, as shown in Fig. 15(a). All show negative curvature during strain hardening, which implies that strong twinning occurred during warm compression.

http://dx.doi.org/10.5772/55597

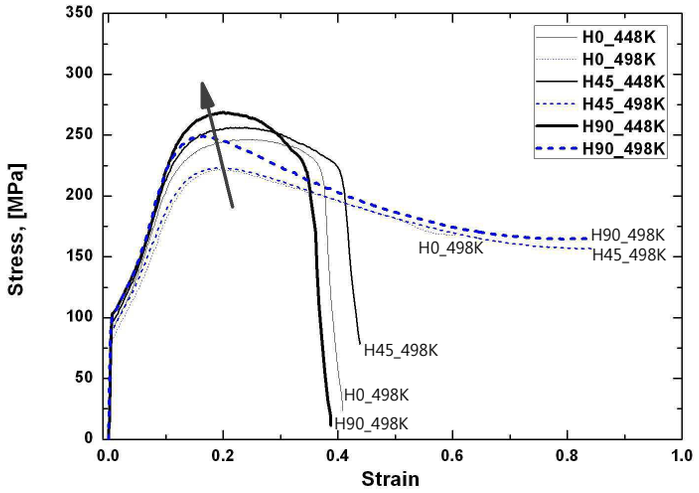

Figure 16. Flow curves obtained from ZK60 alloys along the horizontal direction (see Fig. 2).

4. Recrystallization of Mg alloys

The recrystallization behavior of magnesium alloys was investigated during warm rolling and the subsequent annealing processes. Usually, plastic works of magnesium alloys, including rolling, extrusion, and forming processes, are performed at elevated temperatures. In the previous section, uniaxial compression carried out at various elevated temperatures was discussed. During the warm processing of the samples, dynamic recrystallization can occur depending on the temperature and the total strain. The as-rolled sheets are usually annealed before the next forming process; thus, the texture and microstructure are expected to change. In this section, two different cases of recrystallization - dynamic recrystallization and static recrystallization - are presented. Static recrystallization at the shear band region is also discussed.

4.1. Dynamic recrystallization of hot-rolled AM31 alloys

Large and small grains are mixed as shown in Fig. 17. Particularly, small grains are located between the large grains, which show similar orientations based on the orientation colors and pole figures. It was noted that a shear band forms inside large grains during hot deformation. The small grains are dynamically-recrystallized. Inside the large grains, numerous low-angle grain boundaries with thin black lines and tensile twins, as specified by the red grain boundaries, are also observed.

4.2. Static recrystallization of warm-rolled AZ31B alloys

The warm-rolled sheets show a mixture of large and small grains, as shown in Fig. 18. It appears that the initial large grains are shattered into various sizes of grains during the warm rolling process. During static annealing for 10 min at 573 K (300 °C), the as-rolled structure becomes a fully-recrystallized grain structure, with all grain shapes equi-axed. There exists some variation in the grain sizes of the annealed sheets. The overall textures of both the as-rolled and annealed sheets revealed similar basal fibers. The basal intensity of the as-roll

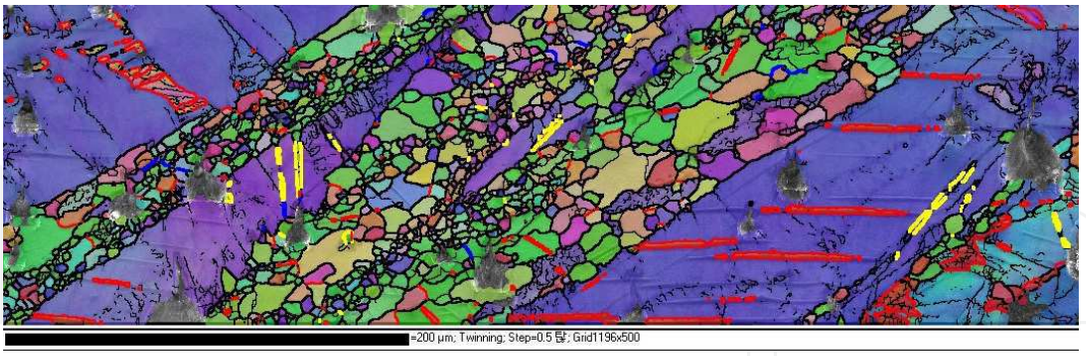

(a)

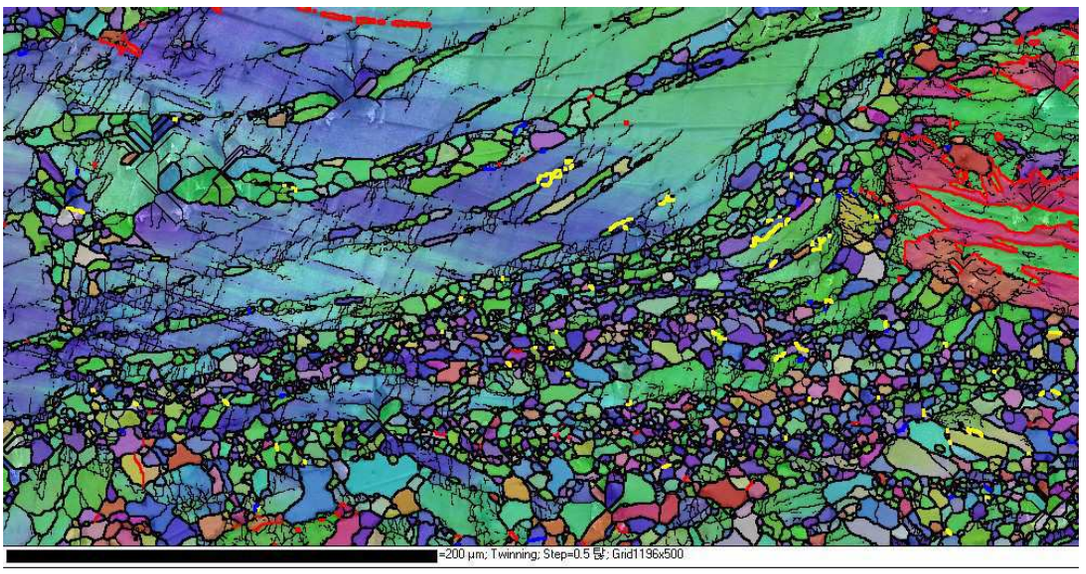

(b)

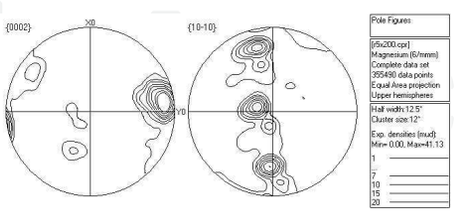

(c)

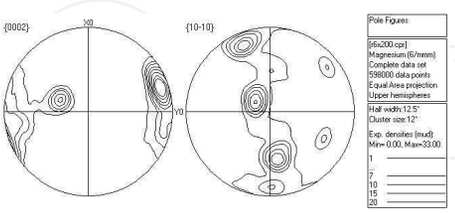

(d)

Figure 17. Inverse pole figure (IPF) maps of hot-rolled AM31 alloys. Two different regions were measured using EBSD. The grain identification angle (GID) is 15° with thick black lines, and the GID is 2° as denoted by the thin black lines. The step size for the EBSD measurements is $0.5\ \mu\mathrm{m}$. The thick red, blue and yellow lines represent the tensile, compressive, and double twin boundaries, respectively. (a) inverse pole figure map and (c) pole figures for the first region. (b) inverse pole figure map and (d) pole figures for the second region.

http://dx.doi.org/10.5772/55597

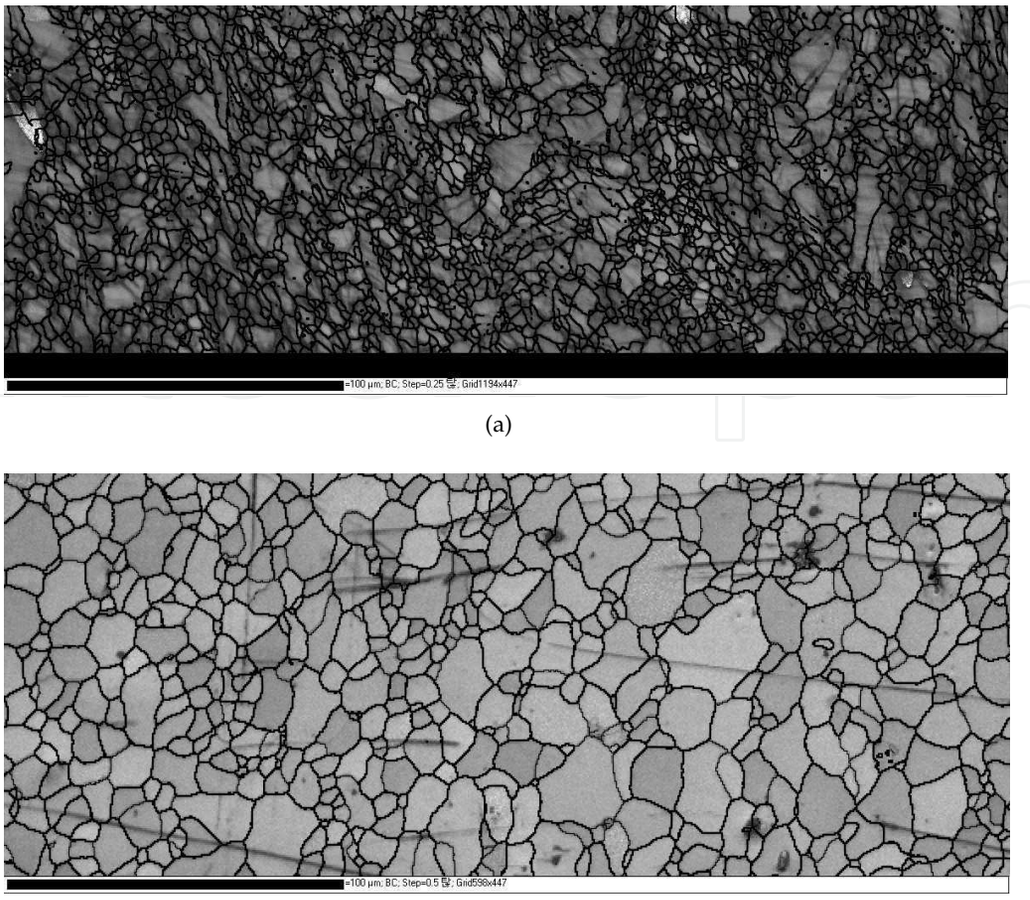

Figure 18. Band contrast maps of warm-rolled AZ31B sheets obtained by means of EBSD measurements. The grain identification angle (GID) is 15° with black lines. The step sizes of the as-rolled and annealed sheets are 0.25 μm and 0.5 μm, respectively. (a) band contrast, and (c) pole figures of the as-rolled sheets. (b) band contrast, and (d) pole figures of the annealed sheets.

sheet confirmed in the (0002) pole figures was stronger than that of the annealed sheet. The basal intensity distribution of the as-rolled sheet also illustrates a more compact distribution than that of the annealed sheet.

Figure 19(a) shows the shear band of the AZ31B alloy, which formed during warm rolling at a temperature of 498 K (225 °C). The shear band region contains numerous twins, and its pole figure in Fig. 19(b) reveals a second strong area of intensity near the X_0 direction. The entire region shows a strong basal texture in Fig. 19(c) of the type usually found during the warm rolling of Mg alloys. The as-rolled sample was annealed for 20 minutes at 573 K (300 °C) and

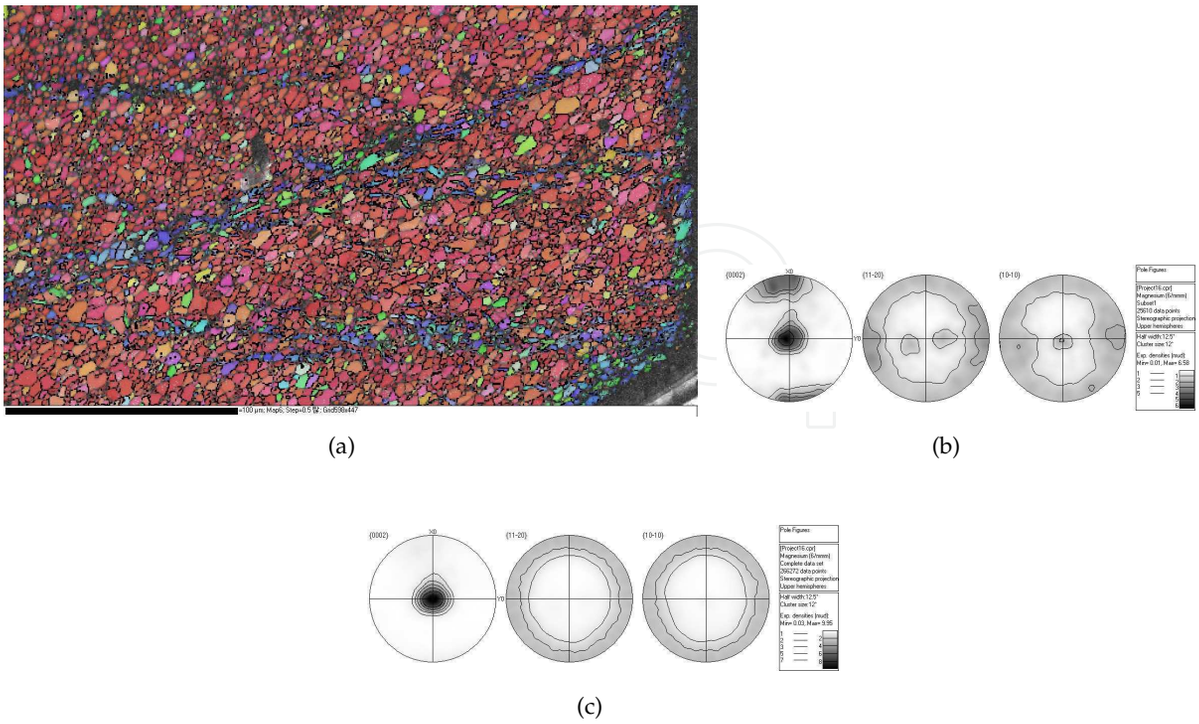

Figure 19. Inverse pole figure maps of warm-rolled AZ31B sheets obtained by means of EBSD measurements. The grain identification angle (GID) is 15° with black lines. The step size is 0.5 μm. (a) inverse pole figure map, (b) pole figures of the shear bands only, and (c) pole figures of the whole region.

was then remeasured using EBSD (Fig. 20). Marked scratch lines were used for the ex-situ mapping. Although the overall region still revealed a basal texture after annealing, a much wider distribution in the basal texture was observed after annealing, as shown in Fig. 20(b), due to the off-basal orientations in the recrystallized shear band region.

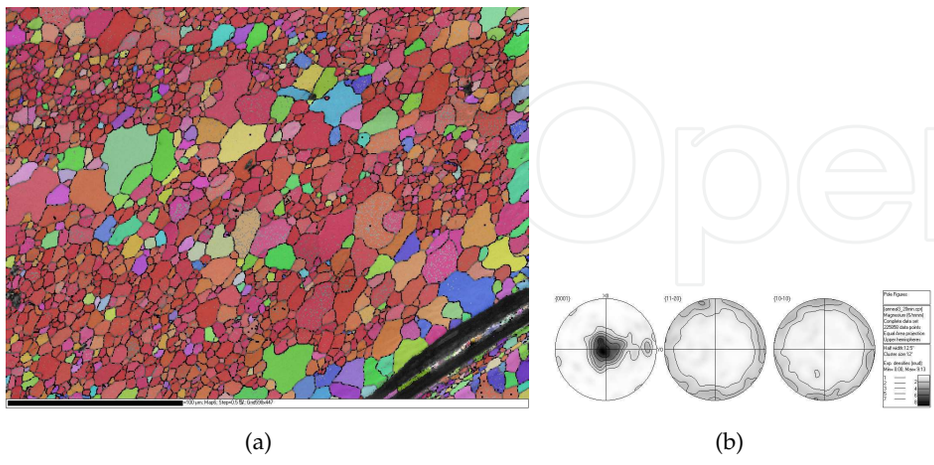

Figure 20. Inverse pole figure masp of warm-rolled AZ31B sheets obtained by means of EBSD measurements. The grain identification angle (GID) is 15° with black lines. The step size is 0.5 μm. (a) inverse pole figure map, and (b) pole figures of the whole region.

5. Conclusion

The textural and microstructural evolution of wrought magnesium alloys of AZ31B, ZK60 and AM31 was investigated during deformation and recrystallization.

- As-extruded AZ31B billets with extrusion fiber orientations show strong twinning during compression along the extrusion direction. Most of the grains went through twinning at a strain of approximately 3%, after which all became a twinned region at a strain of about 8%. As-warm rolled ZK60 alloys with a weak basal texture also show strong twinning during compression along the rolling direction. Both the as-extruded AZ31B and the warm-rolled ZK60 compressed samples were designed to experience c-axis tension during compression, allowing easy activation of tensile twinning. The flow curves revealed that tensile twinning clearly relaxed the strain-hardening behavior, as evidenced by negative curvature.
- The as-casted AM31 alloys with an initial random orientation show that the shear band can provide a useful mechanism to accommodate external loading. Inside large grains, many shear bands form and are recrystallized during the hot rolling process. The as-rolled AZ31B strips fabricated by twin roll casting possessed initial basal fibers that changed into identical basal fibers after full annealing. During the static annealing process, the deformed microstructure became an equi-axed and recrystallized grain structure. The shear band region with off-basal texturing provides off-basal textures during static annealing and contributes to lowering the basal texturing.

Acknowledgements

The authors would like to thank Lili Chang, Yinong Wang, Shou-ren Wang, Sang Su Jeong and Hyoung-Wook Kim for their comments and help.

Author details

Jae-Hyung Cho and Suk-Bong Kang

Korea Institute of Materials Science (KIMS), Light Metals Division, South Korea

References

[1] S. R. Agnew, M. H. Yoo, and C. N. Tome. Application of texture simulation to understanding mechanical behavior of Mg and solid solution alloys containing Li and Y. *Acta Mater.*, 49:4277–4289, 2001.

[2] J. Bohlen, M.R. Nurnberg, J.W. Senn, D. Letzig, and S.R. Agnew. The texture and anisotropy of magnesium-zinc-rare earth alloy sheets. *Acta Mater.*, 55:2101–2112, 2007.

[3] L.W.F. Mackenzie and M. Pekguleryuz. The influences of alloying additions and processing parameters on the rolling microstructures and textures of magnesium alloys. *Mater. Sci. Eng., A*, 480:189–197, 2008.

[4] A.C. Hanzi, F.H. Dalla Torre, A.S. Sologubenko, P. Gunde, R. Schmid-Fetzer, M. Kuehlein, J.F. Loffler, and P.J. Uggowitzer. Design strategy for microalloyed ultra-ductile magnesium alloys. *Philos. Mag. Lett.*, 89(6):377–390, 2009.

[5] L. L. Chang, Y. N. Wang, X. Zhao, and J. C. Huang. Microstructure and mechanical properties in an az31 magnesium alloy sheet fabricated by asymmetric hot extrusion. *Mater. Sci. Eng., A*, 496:512–516, 6 2008.

[6] N. Stanford and M. R. Barnett. The origin of "rare earth" texture development in extruded mg-based alloys and its effect on tensile ductility. *Mater. Sci. Eng., A*, 496:399–408, 5 2008.

[7] J. Koike, T. Kobayashi, T. Mukai, H. Watanabe, M. Suzuki, K. Maruyama, and K. Higashi. The activity of non-basal slip systems and dynamic recovery at room temperature in fine-grained AZ31B magnesium alloys. *Acta Mater.*, 51:2055–2065, 13 2003.

[8] S. H. Kim, B. S. You, C. D. Yim, and Y. M. Seo. Texture and microstructure changes in asymmetrically hot rolled AZ31 magnesium alloy sheets. *Materials letters*, 59:3876–3880, 2005.

[9] X. Gong, S. B. Kang, S. Li, and J. H. Cho. Enhanced plasticity of twin-roll cast ZK60 magnesium alloy through differential speed rolling. *Mater. Des.*, 30:3345–3350, 4 2009.

[10] B. Beausir, S. Biswas, D. Kim, L. Toth, and S. Suwas. Analysis of microstructure and texture evolution in pure magnesium during symmetric and asymmetric rolling. *Acta Mater.*, 57:5061–5077, 13 2009.

[11] X. Gong, L. Hao, S. B. Kang, J. H. Cho, and S. Li. Microstructure and mechanical properties of twin-roll cast Mg-4.5Al-1.0Zn sheets processed by differential speed rolling. *Mater. Des.*, 31:1581–1587, 13 2010.

[12] J. H. Cho, H. M. Chen, Shi-Hoon Choi, Hyoung-Wook Kim, and S.-B. Kang. Aging effect on texture evolution during warm rolling of ZK60 alloys fabricated by twin-roll casting. *Metall. Mater. Trans. A*, 41:2575–2583, 2010.

[13] Jae-Hyung Cho, Hyoung-Wook Kim, Suk-Bong Kang, and Tong-Seok Han. Bending behavior, and evolution of texture and microstructure during differential speed warm rolling of az31b magnesium alloys. *Acta Mater.*, 59:5638–5651, 2011.

[14] A. Jain and S.R. Agnew. Modeling the temperature dependent effect of twinning on the behavior of magnesium alloy AZ31B sheet. *Mat. Sci. and Engr. A*, A462:29–36, 2007.

[15] A. Chapuis and Julian H. Driver. Temperature dependency of slip and twinning in plane strain compressed magnesium single crystals. *Acta Mater.*, 59:1986–1994, 2011.

[16] S.J. Liang, Z.Y. Liu, and E.D. Wang. Microstructure and mechanical properties of Mg-Al-Zn alloy sheet fabricated by cold extrusion. *Mater. Letters*, 62:4009–4011, 13 2008.

[17] L. Y. Wei, G. L. Dunlop, and H. Westengen. The intergranular microstructure of cast Mg-Zn and Mg-Zn-Rare Earth alloys. *Metall. Trans. A*, 26A:1947–1955, 1995.

[18] L. Y. Wei, G. L. Dunlop, and H. Westengen. Precipitation hardening of Mg-Zn and Mg-Zn-RE alloys. *Metall. Trans. A*, 26A:1705–1716, 1995.

[19] X. Gao and J. F. Nie. Characterization of strengthening precipitate phases in a Mg-Zn alloy. *Scripta Materialia*, 56(8):645–648, 2007.

[20] J. H. Cho, Y. M. Jin, H. W. Kim, and S. B. Kang. Microstructure and mechanical properties of ZK60 alloy sheets during aging. *Materials Science Forum*, 558-559:159–164, 2007.

[21] H. Chen, S. B. Kang, H. Yua, J. H. Cho, H. W. Kim, and G. Mina. Effect of heat treatment on microstructure and mechanical properties of twin roll cast and sequential warm rolled ZK60 alloy sheets. *Journal of Alloys and Compounds*, 476:324–328, 2009.

[22] Jae-Hyung Cho, Hyoung-Wook Kim, Suk-Bong Kang, and Sang Soo Jeong. Texture and microstructure evolution during the symmetric and asymmetric rolling of AZ31B magnesium alloys. *Materials science and engineering A*, in press, 2013.

[23] J. H. Cho, A. D. Rollett, and K. H. Oh. Determination of a mean orientation in electron backscatter diffraction measurements. *Metallurgical and materials transactions A*, 36A(12):3427–3438, 2005.

IntechOpen